High-Speed Multi-Modal Extended Depth-of-Field Microscopy with an Electrically Tunable Lens

Runnan Zhang, Ning Zhou, Hanci Tang, Minhao Xia, Zewei Cai, Jiasong Sun, Qian Chen,* and Chao Zuo*

High spatial resolution imaging over the entire volume for intravital imaging of biological specimens has long been vital. However, the depth-of-field (DOF) and spatial resolution are intrinsically interdependent. Here, a new extended DOF (EDOF) microscopy technique based on partially coherent annular illumination is proposed, termed AI-EDOF, by combining an electrically tunable lens with a conventional microscope with modified illumination, for motion-free, high spatial resolution real-time all-in-focus imaging over thick volumes. EDOF imaging is obtained with spatial resolution up to near the incoherent diffraction limit (∼388 nm, 20×/ 0.8NA) and temporal resolution ∼30 fps. Moreover, it is demonstrated that the coupled phase and absorption components of the complex refractive index in optical diffraction tomography microscopy can be solved by focus scanning. The Richardson-Lucy deconvolution with total variation regularization is adopted for deblurring and suppressing noise under low light efficiency high-speed exposure. To demonstrate the capabilities of the proposed method, experiments are conducted using fixed transgenic zebrafish larvae, *Drosophila* larvae and dynamic *Caenorhabditis elegans* under both transmissive and fluorescent imaging modalities, revealing the proposed approach is prospective to be adopted by broad applications such as pharmacokinetics and tumor immunology.

1. Introduction

With the increasingly urgent needs of life science, rapid imaging over large volumes for the in-vivo investigation of highly dynamic biological specimens becomes vital. Conventional light microscopy suffers from a limited depth of field (DOF), which is determined by the focal depth of the objective lens. Only the portions of the specimens within the DOF appear in focus and sharp, while the remaining areas are blurred by the defocus point spread function (PSF) of the system. Furthermore, high resolution is always desired in microscopic imaging, but the high spatial frequency information of optical signals, that is, the larger wave vector angle of the light field, which improves the spatial resolution of the microscopic system, will accelerate the divergence rate of the focus spot and reduce the DOF of the system, resulting in poor imaging quality for 3D thick samples. As a result, in a typical light microscope, high spatial resolution invariably coexists with a small DOF. Emerging techniques that attempt to circumvent these restrictions have been of great interest.

Extended depth-of-field (EDOF) microscopy allows for imaging over large volumes in a straightforward manner. Actually, there exists a diversity of methods for EDOF, each one with its own pros and cons. The coded aperture methods,[1–4] including both amplitude and phase engineering of the pupil function, can achieve DOFs up to a few tens of microns without requiring any movement. However, it often acquires additional hardware such as amplitude or phase mask, and thus the light is inefficient and the DOFs are limited. Light field microscopy[5–9] is a powerful tool for rapid volumetric imaging of weakly scattering or fluorescent specimens. By introducing a microlens array into the light path of a conventional microscope, it is possible to image both the lateral and angular distribution of light passing through the specimen volume. However, the large DOF of the light field is at the expense of spatial resolution, which is subject to microlens array size and sensor pixel resolution. Focus scanning methods[10–16] provide photon-efficient solutions, by mechanical scanning or high-speed instrument such as an electrically tunable lens (ETL), deformable mirror, etc. However, under an incoherent or partially coherent circular illumination scheme, the contrast and resolution of the EDOF imaging are limited.[17–20]

On the other hand, essential benefits provided by partially coherent light microscopy such as improved spatial resolution,

R. Zhang, N. Zhou, H. Tang, M. Xia, Z. Cai, J. Sun, C. Zuo
Smart Computational Imaging Laboratory (SCILab)
School of Electronic and Optical Engineering
Nanjing University of Science and Technology
Nanjing, Jiangsu 210094, China
E-mail: zuochao@njust.edu.cn
R. Zhang, N. Zhou, H. Tang, M. Xia, Z. Cai, J. Sun, Q. Chen, C. Zuo
Jiangsu Key Laboratory of Spectral Imaging & Intelligent Sense
Nanjing University of Science and Technology
Nanjing, Jiangsu 210094, China
E-mail: chenqian@njust.edu.cn
R. Zhang, N. Zhou, H. Tang, M. Xia, Z. Cai, J. Sun, Q. Chen, C. Zuo
Smart Computational Imaging Research Institute (SCIRI), Nanjing University of Science and Technology
Nanjing, Jiangsu 210094, China

The ORCID identification number(s) for the author(s) of this article can be found under https://doi.org/10.1002/lpor.202300770

DOI: 10.1002/lpor.202300770

optical sectioning, and speckle-noise suppression are exploited for optical diffraction tomography (ODT) microscopy.[21–28] However, both phase and absorption information of the complex refractive index of the specimen contribute to the measured intensity,[29] making it challenging to decouple the two contents with a single linear deconvolution filter. To solve this problem, it usually requires two or more datasets of the same object with different illumination functions,[29–31] while these methods result in measurement complexity and computation cost. Another way is to assume the phase-attenuation duality analogous to 2D phase imaging,[32,33] while this assumption is not universal. Due to the fact that the absorption information is non-negligible for diverse biological specimens' structures, we have found that the phase information can be eliminated by focus scanning, and thus the EDOF absorption information is decoupled.

In this paper, we developed an EDOF microscopy technique based on annular illumination, termed AI-EDOF. Specifically, the platform consists of a high-speed ETL located in the Fourier plane of the 4f telecentric module incorporated after the tube lens of the commercial inverted microscope that allows for rapid focus scanning (the highest speed up to ≈1k Hz). We further demonstrated that by replacing the conventional circular illumination aperture with an annular one, the partially coherent matched annular illumination not only strongly boosts the imaging contrast for low spatial frequencies, but improves the practical imaging resolution to the near-incoherent diffraction limit (∼194 nm half pitch, 0.8 NA). We also found that the phase and absorption information, which are coupled at one certain focus plane, can be decoupled by rapid focus scanning due to the odd symmetry of the 3D phase transfer function. Moreover, we adopted a modified form of iterative Richardson-Lucy (RL) deconvolution with a regularization constraint based on total variation,[34,35] which suppresses unstable oscillations while preserving object edges under low light rapid exposure. In addition to quantitative resolution evaluations, we demonstrated its utilities for thick species under both annular illumination imaging and wide-field fluorescent imaging, including transgenic zebrafish larvae and *Drosophila* larvae. We further demonstrated real-time imaging (∼30 fps) of *Caenorhabditis elegans* (*C. elegans*) under multi-modalities, revealing the developed AI-EDOF method is a promising tool for broad applicability in the study of biological dynamics.

2. Method

2.1. Imaging Formation Model of a Partially Coherent Optical Microscope

In general, image formation in microscopic imaging systems can be described by Fourier transforms and a linear filtering operation in the pupil plane:[36] a coherent imaging system is linear in complex amplitude, while an incoherent imaging system is linear in intensity. However, for partially coherent imaging, this process is complicated by the non-linear dependency of the image intensity on the object, light source, and imaging system. For wide-field fluorescent imaging modality, since each fluorescent emission is generally incoherent, the final intensity captured at the image plane can be considered as the intensity superposition of different emissions. However, under bright-field imaging, for a quasi-monochromatic light source, the spatial coherence of illu-

mination is manipulable and is essential for DOF, imaging contrast, spatial resolution, etc.

Considering the standard 6f optical setup shown in **Figure 1a**, in which an incoherent delta-correlated light source (the condenser exit pupil) illuminates an object (with a complex transmittance $t(\mathbf{x}) = a(\mathbf{x}) \exp[i\phi(\mathbf{x})]$, where $\mathbf{x}$ is the two-dimensional (2D) spatial coordinates in the real space, and $a(\mathbf{x})$ and $\phi(\mathbf{x})$ are absorption and phase, respectively), which is imaged using an objective lens. This configuration of the so-called Köhler illumination and telecentric detection can be applied to almost all bright-field microscopic configurations.

Considering the illumination emerging from a light source with intensity distribution $S(\mathbf{u})$ in the aperture diaphragm plane (where $\mathbf{u}$ is the corresponding 2D coordinate in the Fourier space), the image $I(\mathbf{x})$ of the object captured at the image plane can be described by (see Supporting Information S1 for detailed derivation):[17,18]

$$I(\mathbf{x}) = \iiint S(\mathbf{u}) T(\mathbf{u}_1) T^*(\mathbf{u}_2) P(\mathbf{u} + \mathbf{u}_1) P^*(\mathbf{u} + \mathbf{u}_2)$$
$$\times \exp\left[i2\pi\mathbf{x}(\mathbf{u}_1 - \mathbf{u}_2)\right] d\mathbf{u}_1 d\mathbf{u}_2 d\mathbf{u} \tag{1}$$

where $P(\mathbf{u})$ is the coherent transfer function corresponding to the objective pupil, and $T(\mathbf{u})$ is the Fourier spectrum of $t(\mathbf{x})$. Due to the superposition of intensities, the observed intensity is not linear in the specimen transmittance. The intensity spectrum consists of a mixing of pairs of spatial frequencies in the amplitude spectrum of the specimen. Such a dependence of the image intensity on the amplitude of the specimen is called "bi-linear" (i.e., linear in pairs) dependence. Separating the contribution of the specimen and system leads to the notion of the transmission cross-coefficient (TCC):[17,18,37,38]

$$TCC(\mathbf{u}_1, \mathbf{u}_2) = \iint S(\mathbf{u}) P(\mathbf{u} + \mathbf{u}_1) P^*(\mathbf{u} + \mathbf{u}_2) d\mathbf{u} \tag{2}$$

To simplify the mathematical formulation, the weak object approximation is often applied to linearize the imaging formation. The complex transmittance of a weak object can be represented as:

$$t(\mathbf{x}) \equiv a(\mathbf{x}) \exp\left[i\phi(\mathbf{x})\right] \approx a(\mathbf{x})[1 + i\phi(\mathbf{x})] \tag{3}$$

It now becomes obvious that the image contrast due to the absorption and phase are decoupled and linear (see Supporting Information S1). We denote the $TCC(\mathbf{u}, \mathbf{0})$, the linear part of the TCC, as the weak object transfer function (WOTF):[18,39]

$$WOTF(\mathbf{u}) \equiv TCC(\mathbf{u}, \mathbf{0}) = \iint S(\mathbf{u}') P(\mathbf{u}' + \mathbf{u}) P^*(\mathbf{u}') d\mathbf{u}' \tag{4}$$

Figure 1b shows the geometric illustrations for deriving the WOTF, given by the overlap of the objective pupil and the displaced source. The WOTF is then given by the weighted area of overlap of $S(\mathbf{u}')P^*(\mathbf{u}')$ and $P(\mathbf{u}' + \mathbf{u})$. The in-focus WOTFs under different spatial coherence (define coherent parameter $S = NA_{ill}/NA_{obj}$, where NA_{ill} and NA_{obj} are the numerical apertures of the illumination and objective lens) are shown in Figure 1c, where the normalized cut-off frequency (normalized by NA_{obj}/λ)
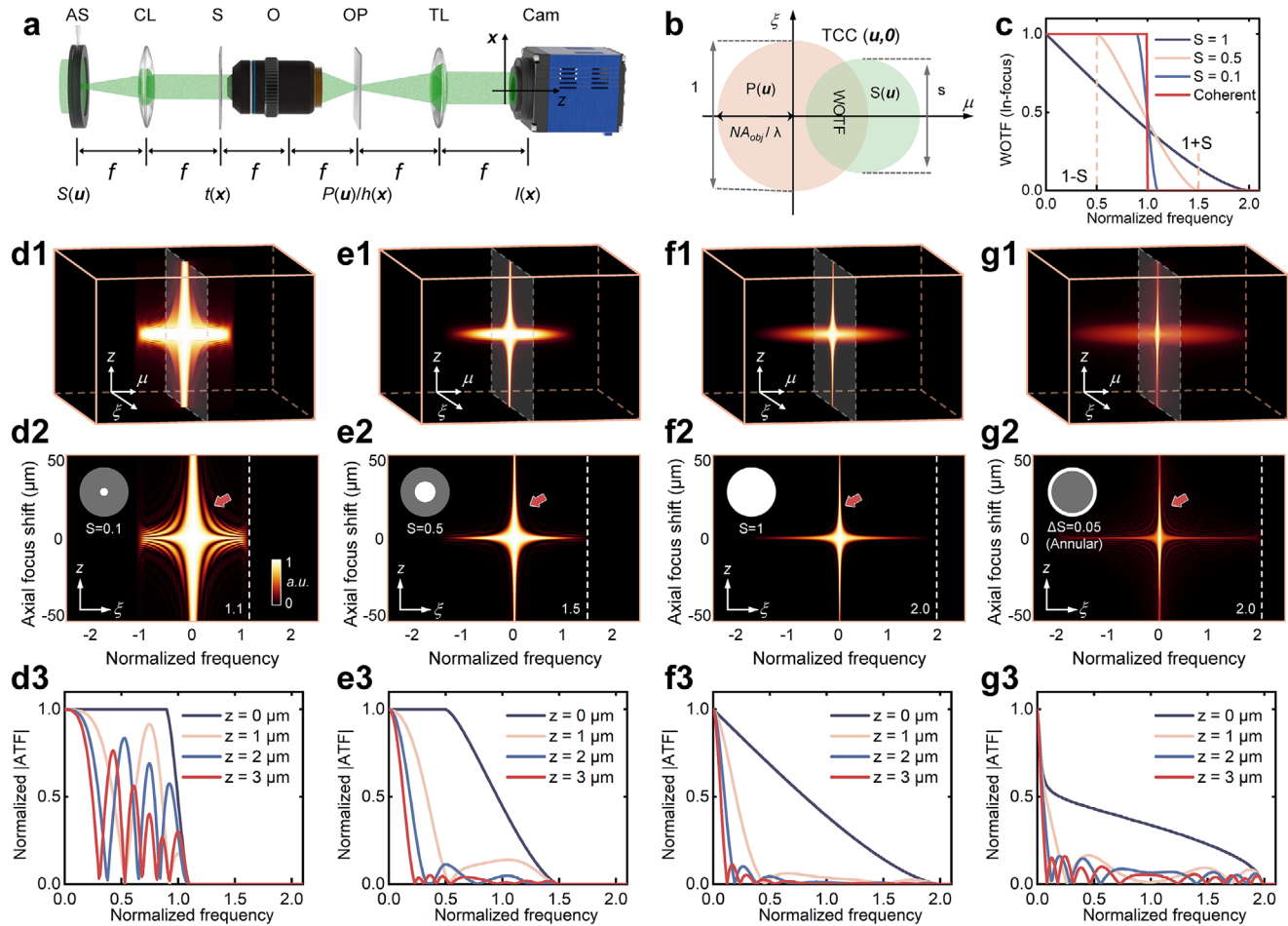
Figure 1. Image formation theory in a partially coherent microscope. a) The 6f Köhler illumination and telecentric imaging system. The condenser diaphragm can be regarded as an incoherent extended source with a finite size. AS, aperture diaphragm (source); CL, condenser lens; S, sample; O, objective; OP, objective pupil; TL, tube lens; Cam, camera. b) Geometric interpretation of the TCC and WOTF. c) The in-focus WOTFs under different spatial coherence. d1–d3) The defocus $|ATF|$ under circular illumination with $S = 0.1$. e1–e3) The defocus $|ATF|$ under circular illumination with $S = 0.5$. f1–f3) The defocus $|ATF|$ under circular illumination with $S = 1$. g1–g3) The defocus $|ATF|$ under annular illumination with $S = 1$, $\Delta S = 0.05$.

is extended from 1 under coherent illumination to $1 + S$ under partially coherent illumination, when $S \geqslant 1$ the cut-off frequency is extended to the incoherent diffraction limit. When the system is in focus, the WOTF can be represented analytically, as given in refs. [17, 18, 39].

Considering the axial defocus into the transfer function:

$$P(\mathbf{u}) = |P(\mathbf{u})| \exp\left(ikz\sqrt{1 - \lambda^2|\mathbf{u}|^2} \right), \ |\mathbf{u}| \leqslant \lambda^{-1} \quad (5)$$

where z is the defocus distance along the optical axis. Substituting Equation (5) into Equation (4) results in a defocus WOTF. The transfer functions for absorption and phase component of a weak object are then given by the real and imagery part of WOTF, respectively:

$$ATF_z(\mathbf{u}) = \mathrm{Re}\left[WOTF(\mathbf{u}) \right] \quad (6)$$

$$PTF_z(\mathbf{u}) = -\mathrm{Im}\left[WOTF(\mathbf{u}) \right] \quad (7)$$

Although the cut-off spatial frequency can be extended up to twice with decreasing spatial coherence (with S from 0 to 1) compared with coherent illumination, two intrinsic limitations are inevitable. First, as shown in Figure 1c, the imaging contrast of different spatial frequency information for a coherent transfer function is a constant, while the imaging contrast for a partially coherent transfer function decreases in the spatial frequency range from $1 - S$ to $1 + S$, resulting in an extremely low high-frequency imaging contrast. Second, as shown in Figures 1d–f, the defocus transfer function $|ATF_z(\mathbf{u})|$ decays rapidly with decreasing spatial coherence, especially under incoherent imaging, and the $|ATF_z(\mathbf{u})|$ goes to zero rapidly as the spatial frequency increases in the small-defocus regime (this also explains why incoherent imaging has a small DOF), leading to attenuation and blurring in small-scale features. As an alternative to the circular illumination pattern, as shown in Figures 1g1–g3, the annular illumination with matched NA not only increases the imaging contrast for high spatial frequencies but also improves the defocus response to near-incoherent diffraction limit spatial resolution.
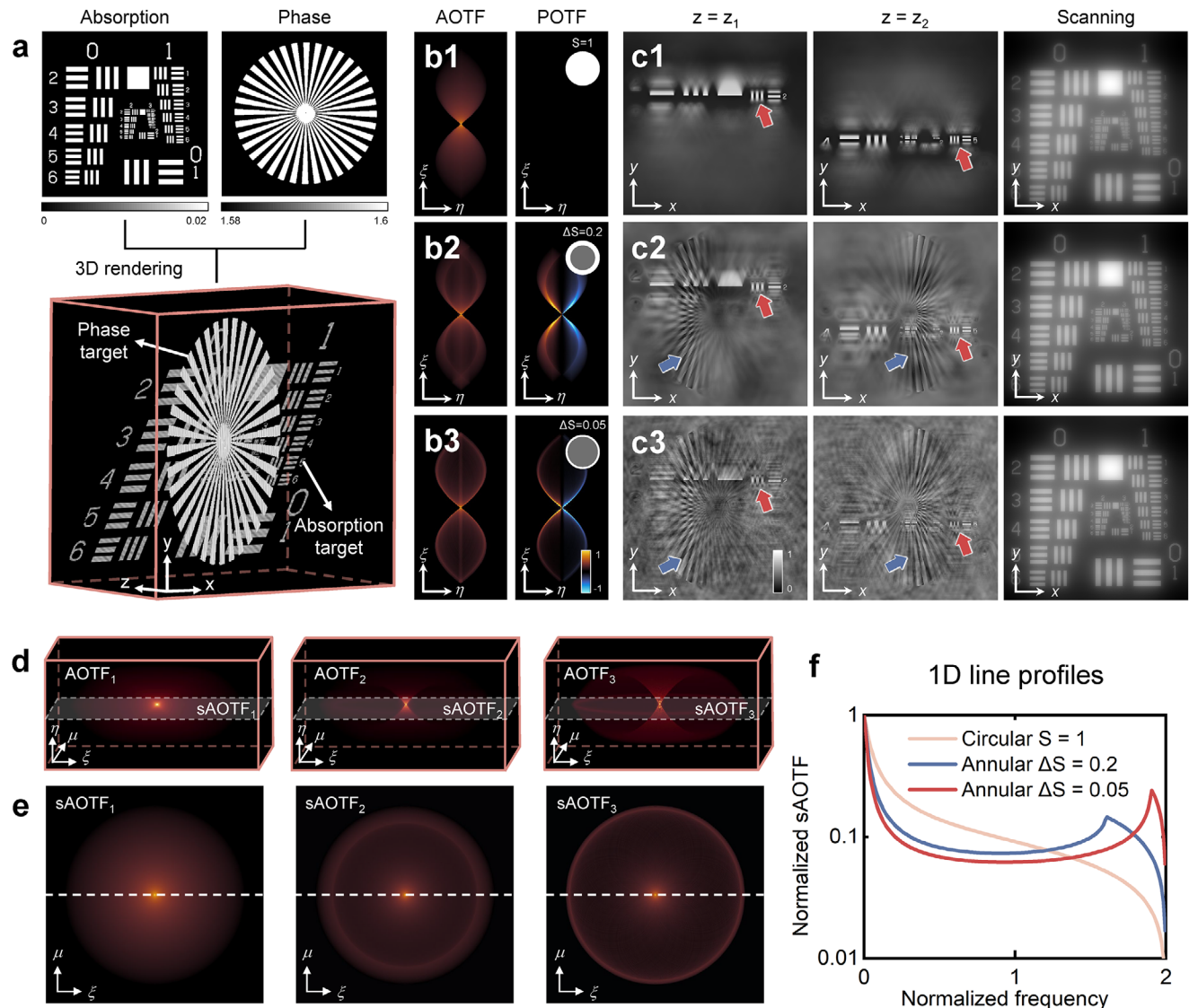
Figure 2. 3D ODT image formation theory in a partially coherent microscope. a) A 3D object composed of absorption (a tilted USAF target) and phase (a tilted star target). b1–b3) The 2D η - ξ section of 3D AOTFs and POTFs under circular illumination with $S = 1$ and annular illumination with $\Delta S = 0.2$ and $\Delta S = 0.05$, respectively. c1–c3) The intensities at two certain image planes z_1 and z_2, the absorption and phase of which are coupled. The single shot all-in focus scanning intensity is left for the absorption part only. d) The 3D AOTFs visualization for (b1)–(b3). e) The single-shot AOTFs, corresponding to the central slice of 3D AOTFs in (d). f) 1D line profiles of sAOTFs in (e), respectively.

2.2. Transport of Intensity Diffraction Tomography Under Partially Coherent Illumination

In the 2D theory of optical imaging, as described above, a thin object is usually represented as a 2D complex transmittance function $t(\mathbf{x}) = a(\mathbf{x}) \exp[i\phi(\mathbf{x})]$ composed of absorption component and phase component. The complex amplitude distribution of the transmitted field is given by the product of the complex amplitude of the incident illumination and the complex transmittance of the object. When we image a 3D object, it is straightforward to extend it to 3D imaging formation, that is, 3D optical diffraction tomography (ODT). A 3D specimen can be characterized by its scattering potential $f(\mathbf{r}) = k_0^2[n_0^2 - n^2(\mathbf{r})]$,[40] where: $\mathbf{r} = (x, y, z)$ is the spatial coordinate, $k_0 = 2\pi/\lambda_0$ with λ_0 being the free-space

wavelength, while $n(\mathbf{r}) = n_{\mathrm{Re}}(\mathbf{r}) + i n_{\mathrm{Im}}(\mathbf{r})$ and n_0 are the refractive index (RI) of the specimen and its surrounding medium, correspondingly. The real part of the RI, $n_{\mathrm{Re}}(\mathbf{r})$ describes how phase delays accumulate as light passes through the sample, while the imaginary part, $n_{\mathrm{Im}}(\mathbf{r})$, describes absorption. We constructed a 3D object as shown in **Figure 2a**, and the tilted absorption target and phase target intersect in 3D space.

To evaluate the phase and absorption effects separately, we consider the real and imaginary parts of the scattering potential $f(\mathbf{r}) = P(\mathbf{r}) + iA(\mathbf{r})$. N. Streibl[29] derived that the 3D intensity images in a bright-field microscope can be written as a linear superposition of the real and imaginary parts of the scattering potential convolved with the corresponding phase and absorption PSFs. It can be straightforwardly interpreted in the reciprocal Fourier

domain. Specifically, the 3D image spectrum, calculated as the 3D Fourier transform of the 3D intensity images, is given by:

$$\hat{I}(\mathbf{u}) = B\delta(\mathbf{u}) + H_A(\mathbf{u})\hat{A}(\mathbf{u}) + H_P(\mathbf{u})\hat{P}(\mathbf{u}) \tag{8}$$

where $\mathbf{u}$ is the frequency corresponding to $\mathbf{r}$, $H_P(\mathbf{u})$ and $H_A(\mathbf{u})$ are the phase (POTF) and absorption (AOTF) optical transfer functions, and $B\delta(\mathbf{u})$ is the background term. Note that the POTF and the AOTF are the 3D Fourier transform of phase PSF and absorption PSF, respectively. The analytic expressions for the POTF and AOTF of a bright-field transmission microscope are:[18,29,41]

$$H_A(\boldsymbol{\mu}, \eta) = \frac{\lambda}{4\pi} \iint P\left(\boldsymbol{\mu}' + \frac{\boldsymbol{\mu}}{2}\right) P^*\left(\boldsymbol{\mu}' - \frac{\boldsymbol{\mu}}{2}\right)$$
$$\times \left[S\left(\boldsymbol{\mu}' + \frac{\boldsymbol{\mu}}{2}\right) + S\left(\boldsymbol{\mu}' - \frac{\boldsymbol{\mu}}{2}\right)\right]$$
$$\times \delta\left[\eta + \sqrt{\lambda^{-2} - \left(\boldsymbol{\mu}' + \frac{\boldsymbol{\mu}}{2}\right)^2}\right.$$
$$\left. - \sqrt{\lambda^{-2} - \left(\boldsymbol{\mu}' - \frac{\boldsymbol{\mu}}{2}\right)^2}\right] d^2\boldsymbol{\mu}' \tag{9}$$

$$H_P(\boldsymbol{\mu}, \eta) = \frac{i\lambda}{4\pi} \iint P\left(\boldsymbol{\mu}' + \frac{\boldsymbol{\mu}}{2}\right) P^*\left(\boldsymbol{\mu}' - \frac{\boldsymbol{\mu}}{2}\right)$$
$$\times \left[S\left(\boldsymbol{\mu}' + \frac{\boldsymbol{\mu}}{2}\right) - S\left(\boldsymbol{\mu}' - \frac{\boldsymbol{\mu}}{2}\right)\right]$$
$$\times \delta\left[\eta + \sqrt{\lambda^{-2} - \left(\boldsymbol{\mu}' + \frac{\boldsymbol{\mu}}{2}\right)^2}\right.$$
$$\left. - \sqrt{\lambda^{-2} - \left(\boldsymbol{\mu}' - \frac{\boldsymbol{\mu}}{2}\right)^2}\right] d^2\boldsymbol{\mu}' \tag{10}$$

where $\boldsymbol{\mu}$ is the frequency with respect to x and y, η is the frequency with respect to z, $S(\boldsymbol{\mu})$ and $P(\boldsymbol{\mu})$ are the source and objective aperture functions, * indicates the complex conjugate, and δ is the Dirac delta function. Since POTF and AOTF only depend on the source $S(\boldsymbol{\mu})$ and pupil $P(\boldsymbol{\mu})$, which are known, they can be pre-computed.

It is well-known that the coherence of the illumination is important for achieving high-quality images. In the previous research, the illumination aperture $S(\boldsymbol{\mu})$ is only restricted to circular shapes. This assumption is well coincident with the Köhler illumination configuration, in which a variable circular diaphragm is used for controlling the spatial coherence of the illumination. However, it should be also noted that the shape of condenser aperture diaphragm can also be manipulated to optimize the form of OTFs, thus allowing for improved imaging performance.[17] We adopted a uniform annular source $S_{annu}(\boldsymbol{\mu})$, the numerical aperture of which is matched with the objective. The source functions are given as:

$$S_{circ}(\boldsymbol{\mu}) = \begin{cases} 1, & if \ |\boldsymbol{\mu}| \leqslant \rho_s \\ 0, & if \ |\boldsymbol{\mu}| > \rho_s \end{cases}, \quad S_{annu}(\boldsymbol{\mu}) = \begin{cases} 0, & if \ |\boldsymbol{\mu}| < \rho_a \\ 1, & if \ \rho_a \leqslant |\boldsymbol{\mu}| \leqslant \rho_b \\ 0, & if \ |\boldsymbol{\mu}| > \rho_b \end{cases} \tag{11}$$

and the pupil function is given as:

$$P(\boldsymbol{\mu}) = \begin{cases} 1, & if \ |\boldsymbol{\mu}| \leqslant \rho_p \\ 0, & if \ |\boldsymbol{\mu}| > \rho_p \end{cases} \tag{12}$$

Figure 2b demonstrates the OTFs under different bright-field engineered coherence illumination (circular $S = 1$, annular $\Delta S = 0.2$, $\Delta S = 0.05$ with matched illumination). As shown in Figure 2b1, the energy is mostly concentrated at the low-frequency response of 3D AOTF, and POTF is inexistent under circular illumination $S = 1$. As shown in Figures 2b2,b3, while annular illumination is performed, the high-frequency responses of AOTF tend to be more and POTF is inevitable due to partially coherent illumination. The high-frequency component accounts for more if the thickness of the annulus becomes narrower.

The 3D OTFs given by Equations (9) and (10) reveals that the 3D OTFs have a significant degree of spatial symmetry under symmetric illumination. All of the OTFs have a generally circular symmetry about the z axis and all of the OTFs generally have near-zero value outside the region of cuff-off frequency. The AOTFs and POTFs (as shown in Figures 2b1 and b3, respectively), have a generally odd and even symmetry along the z axial. For single-shot all-in-focus imaging, the captured 2D all-in-focus PSF is the sum of 3D PSF along the z axis. According to the Fourier slice theorem, the scanning transfer function for both absorption [sAOTF, $sH_A(\boldsymbol{\mu})$] and phase [sPOTF, $sH_P(\boldsymbol{\mu})$], that is, the Fourier spectrum of 2D all-in-focus PSF, can be seen as the central slice of 3D OTF. Here, we can decouple the absorption information based on this property. Moreover, this property is also essential for incoherent fluorescent computed tomography imaging[9] (see Supporting Information S3 for details).

$$sH_A(\boldsymbol{\mu}) = H_A(\boldsymbol{\mu}, \eta)\big|_{\eta=0} = H_A(\boldsymbol{\mu}, 0) \tag{13}$$

$$sH_P(\boldsymbol{\mu}) = H_P(\boldsymbol{\mu}, \eta)\big|_{\eta=0} = H_P(\boldsymbol{\mu}, 0) \tag{14}$$

As a result, according to the symmetry, the phase contribution vanishes in the single-shot all-in-focus image, and only the absorption part is recorded so that the coupled phase and absorption are solved. We only have to consider the sAOTF. As illustrated in Figure 2c1, when the coherent parameter of circular illumination $S \geqslant 1$, the captured 3D intensities at a certain plane z_1 or z_2 only consist of absorption information and the DOF is limited. The scanning intensity can get all-in-focus absorption information. As illustrated in Figures 2c2,c3, when the annular illumination scheme is adopted, although the DOF of annular illumination is larger than that of the circular illumination (as shown in the last section), the absorption and phase are coupled in the captured 3D intensities at a certain plane z_1 or z_2, which makes the deconvolution process much more complicated. The scanning intensity decouples the absorption component and gives all-in-focus absorption information. Therefore, we only have to take AOTF into consideration. The 3D AOTFs of different spatial coherence are shown in Figure 2d, and the sAOTFs, which are the central slices of 3D AOTFs according to the Fourier slice theorem, are shown in Figure 2e. The corresponding 1D line profiles as shown in Figure 2f are plotted

to compare the frequency responses of sAOTF1, sAOTF2 and sAOTF3, respectively. The highest frequency response (as the arrows in the figure point to) becomes larger if the thickness of the annulus becomes narrower. The radius of the annulus will determine the cut-off frequency, and the thickness of the annulus will affect the frequency response, and we have made detailed discussions in Supporting Information S2. It can be deduced that we should choose the annulus whose diameter equal that of the objective pupil and make its thickness as small as possible to optimize both frequency response and imaging resolution. However, if the annulus width is too narrow, the frequency response is steep at certain high frequencies. Therefore, the appropriate width should be chosen, and it will be discussed in the following section.

2.3. Richardson–Lucy Deconvolution with Total Variation Regularization

Although the rapid focus scanning collects all focus information, the captured single-shot image is still degraded by out-of-focus light of each layer and by Poisson noise due to photon-limited detection, especially under rapid exposure conditions. While the deconvolution method tends to amplify noise, the usage of image priors-based regularization constraints has to be applied to reduce the noise sensitivity. Here, we combine the iterative RL algorithm,[34,35,42] which computes the maximum likelihood estimation adapted to Poisson statistics, with a regularization constraint based on Total Variation (RL-TV) to suppress unstable oscillations while preserving object edges. The RL-TV deconvolution is derived as (see Supporting Information S5 for details):

$$o_{k+1}(\mathbf{x}) = \left\{ \left[\frac{i(\mathbf{x})}{(o_k \otimes h)(\mathbf{x})} \otimes h(-\mathbf{x}) \right] \right\} \times \frac{o_k(\mathbf{x})}{1 - \varepsilon_{TV} div \left(\frac{\nabla_{o_k}(\mathbf{x})}{\left| \nabla_{o_k}(\mathbf{x}) \right|} \right)} \tag{15}$$

where $div(\cdot)$ stands for the divergence, $i(\mathbf{x})$ represents the captured intensity, $o_k(\mathbf{x})$ is the recovered object function under k^{th} iteration, which is often constrained with non-negativity prior, $\nabla_{o_k}(\mathbf{x})$ stands for the gradient of $o_k(\mathbf{x})$, ε_{TV} represents the regularization parameter, and $h(\mathbf{x})$ is the PSF of the optical system $(h(\mathbf{x}) = \mathcal{F}^{-1}\{sH_A(\boldsymbol{\mu})\})$ with non-negativity prior. Numerically we noticed that the regularization parameter ε_{TV} should be neither too small nor too large: if ε_{TV} is too small, RL will be dominated by the data model; if ε_{TV} is too large, RL will be dominated by the regularization term. For larger ε_{TV}, the denominator of Equation (15) will become zero or negative. This must be avoided because small denominators create points of very high intensity, which are amplified at each iteration. Typically, the value of ε_{TV} varies from 0 to 0.01 according to the practical noise level of the imaging system. A negative value violates the nonnegativity constraint. The stop criterion is usually defined by Equation (S46)(See Supporting Information S5 for details). The comparisons between iterative deconvolution and direct deconvolution (such as Wiener deconvolution) methods under different noise levels are discussed in Supporting Information S6.

3. Results

3.1. Experimental Setup

Figure 3a demonstrates our experimental system. We modified a basic microscopy setup with both transmissive bright-field and fluorescent imaging modalities (IX81, Olympus) to incorporate a 4f system containing an ETL (EL-16-40-TC-VIS-20D-C-E, Optotune) and two achromatic doublets with equal focal length ($f1 = f2 = 100$ mm) in the detection path to conjugate the native image plane (NIP) into a cooled sCMOS camera (pco.edge 4.2, PCO GmbH, 2048 × 2048 pixel resolution, 6.5 μm pixel size) for rapid focus scanning and an additional programmable LED array for bright-field illumination coherence engineering.

Considering the Fourier transform property of the 4f system, the variation of ETL's focal power located at the Fourier plane is equivalent to adding a quadratic phase modulation:[43]

$$t_l(\mu, \xi) = \exp\left[-\frac{i\pi}{\lambda f_{eff}} (\mu^2 + \xi^2) \right] \tag{16}$$

where (μ, ξ) is the spatial coordinates in the Fourier plane of the 4f system, and f_{eff} is the effective focal length of ETL controlled by current. From the angular spectrum perspective, the free-space propagation distance Δz of the wavefield is given by ref. [36] (see Supporting Information S4 for details):

$$\Delta z = -\frac{1}{M^2} \frac{n \cdot f^2}{f_{eff}} \tag{17}$$

where M is the magnification of the objective, n is the refractive index of the immersion medium, and f is the focal length of two Fourier lenses. Since f_{eff} can be electronically controlled, the defocus distance Δz can be easily adjusted.

Furthermore, it should be noted that the precise alignment of the ETL is critical and therefore it is mounted on a translator. The accurate position of the ETL along the optical axis ensures the magnification and lateral shift are invariantly independent of the focal power of ETL. Considering allowable misalignment of ETL, we made pre-calibration of the imaging system's PSF, considering axial focus shift, magnification, and lateral shift among the whole focal range as shown in Figure 3b.

3.2. AI-EDOF Experimental Results of a Tilted USAF Resolution Target

To quantitatively verify the performance of our experimental system and the RL-TV deconvolution method, we first performed experiments on a USAF resolution target. We used a 20×/0.8NA objective (Olympus) and an additional ×2 magnification lens to avoid the pixel aliasing problem. An absorption resolution target (Ready Optics Company, USA) is tilted in the 3D space with angle $\theta \approx 25°$ to form a 3D volume, as shown in **Figure 4a**, and the 3D volume is recovered by 3D RL deconvolution for visualization. The proposed EDOF method was compared with the traditional circular illumination ($S = 1$) and partially coherent matched annular illumination with different widths ($\Delta S = 0.2$ and $\Delta S = 0.05$). We captured the scanning all-in-focus
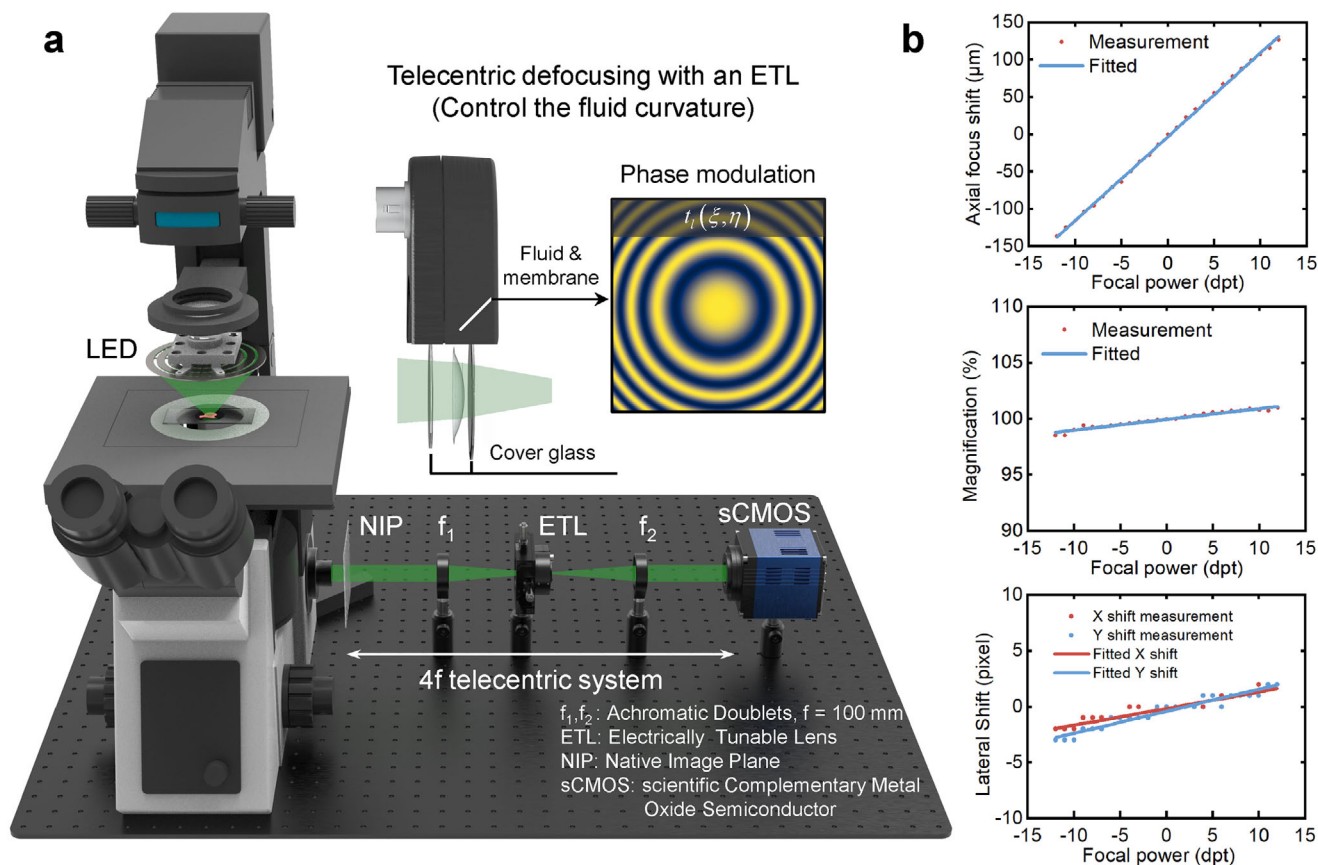
ADVANCED
SCIENCE NEWS

www.advancedsciencenews.com

LASER
& PHOTONICS
REVIEWS

www.lpr-journal.org

Figure 3. Optical setup of EDOF platform and its pre-calibration. a, A 4f telecentric system with ETL located at the Fourier plane is attached to Olympus IX81 bright field microscope. The Fourier lens f1 relays the native image plane (NIP) onto the ETL. Fourier lens f2 reconstructs the final image at the sCMOS sensor, which is conjugated with the image plane. A programmable LED array is used for bright-field illumination. The shift of the NIP with nearly equal magnification can be realized by adjusting the focal length of ETL. b, The fitted pre-calibration curve between the focal power of ETL and axial focus shift, magnification and lateral shift.

single-shot intensity images as shown in Figures 4b1–b3 under different illuminations and performed RL-TV deconvolution, respectively. The zoom-in regions of interest (ROIs) give clear insights into captured images. It can be seen that under circular illumination, the captured image is highly blurred, while the images under annular illumination contain more high-frequency information. The resolution of deconvolved images under circular illumination compared with matched annular illumination is limited due to the relatively low high-frequency response in the sAOTF (Figure 2e). However, although the high-frequency response is enhanced, if the annular widths are extremely narrow, the deconvolved image contrast will be inappropriate and more easily corrupted by noise. Comparing Figure 4b2 with Figure 4b3, and their 1D line profiles as shown in Figures 4c1,c2, we can see that the intensity of low-frequency information (as shown in Figure 4c1) of $\Delta S = 0.05$ is lower than $\Delta S = 0.2$, and it is more easily to be corrupted by high-frequency noise, while the image contrast of $\Delta S = 0.2$ is more balanced. As shown in Figure 4c2, the achieved highest resolution after deconvolution under circular illumination is 488 nm (Group 11, Element 1), which is enhanced to 388 nm (Group 11, Element 3) by matched annular illumination after deconvolution and agrees well with the theoretical incoherent diffraction limit of 388 nm (NA = 0.8). Overall,

taking both imaging resolution and contrast into consideration, we selected the matched annular illumination with $\Delta S = 0.2$ for the following biological experiments.

3.3. Dual-Modal EDOF Imaging of Transgenic Zebrafish Larvae and *Drosophila* Larvae

We demonstrated the capabilities of AI-EDOF by imaging the fixed transgenic zebrafish larvae *Tg(fli1:eGFP)* and *Drosophila* larvae, and the EDOF results under annular illumination, wide-field fluorescent imaging, and two modalities overlay are shown in **Figure 5**. For restrained experiments, the zebrafish larvae were embedded in 1pr low melting point agarose and imaged by a 10×/0.4NA objective (Olympus). The whole axial scanning range is ~300 μm (z = −150 to 150 μm) and the selected field of view is 450 × 450 μm². The captured raw image (Figure 5a1) has a limited DOF at a single focus plane (z = 10 μm), and the single-shot focus scanning image under annular illumination is shown in Figure 5a2. The AI-EDOF absorption information recovered by RL-TV deconvolution is shown in Figure 5a3. The retina, hindbrain and otic capsule can be clearly seen in Figure 5a3 while they are blurred in Figure 5a2. The captured raw image (Figure 5b1)
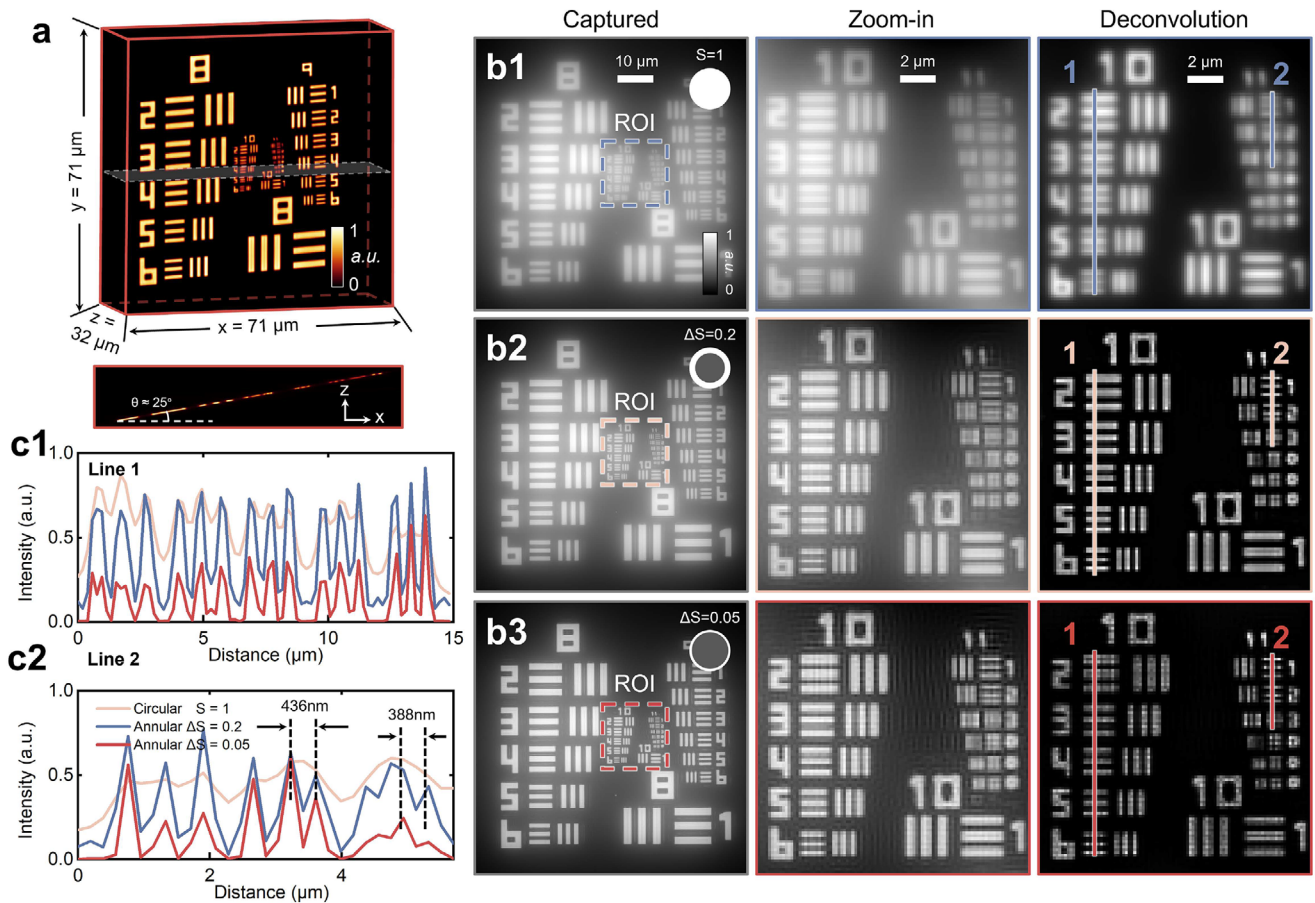
Figure 4. The EDOF experimental results of a tilted USAF resolution target under different illuminations using RL-TV deconvolution. a) The initial tilted 3D volume calculated by 3D RL deconvolution. b1–b3) The captured images and deconvolution results under circular and annular illuminations, respectively. c1,c2) The corresponding line profiles of 1 and 2 in the deconvolution images are shown to compare the imaging resolution and contrast.

has a limited DOF at a single focus plane (z = 0 μm) under wide-field fluorescent imaging, and the single-shot focus scanning image under wide-field fluorescent imaging is shown in Figure 5b2. The corresponding deconvolution EDOF result is shown in Figure 5b3. The forebrain, midbrain, hindbrain, eye, hatching gland and neural tube are visible. It demonstrated that the zebrafish larvae are on the 20-somite segmentation period (19 hpf, hours post fertilization). The enlarged ROI1 and ROI2 show the effectiveness of EDOF and the deconvolution method. The overlay of two imaging modalities shows the label-free absorption information and labeled fluorescent information simultaneously. Next, we imaged a fixed *Drosophila* larvae specimen under a 40×/0.6NA objective (Olympus). The whole axial scanning range is ~80 μm (z = −40 to 40 μm) and the selected field of view is 150 × 150 μm². The captured raw image (Figure 5d1) has a limited DOF at a single focus plane (z = −5 μm) and the single-shot focus scanning image under annular illumination is shown in Figure 5d2. The corresponding deconvolution absorption information is shown in Figure 5d3. The tibiotarsi of *Drosophila* larvae's leg is clearly recovered. The captured raw image (Figure 5e1) has a limited DOF at a single focus plane (z = 5 μm) under wide-field fluorescent imaging, and the single-shot focus scanning image under wide-field fluorescent imaging is

shown in Figure 5e2. The corresponding deconvolution EDOF result is shown in Figure 5e3. The tarsal segment and ectopic muscle fibers are clearly visible. The enlarged ROI3 and ROI4 also visualize the image at a single focus plane, all-in-focus image and deconvolution results. The total variation parameter ε_{TV} was empirically chosen as 0.001 and 0.01 under annular illumination and fluorescent imaging modality considering both detail perseveration and noise suppression, respectively. The overlay of two modalities as shown in Figure 5f shows complementary information.

3.4. Dynamic Multi-Modal Imaging of *C. elegans*

Our final experiment demonstrates the dynamic imaging capabilities of AI-EDOF on a *C. elegans* (TJ356) in **Figure 6** and Videos S1 and S2, Supporting Information. The whole experiments were performed under a 40×/ 0.75NA objective (Olympus). As can be seen from Figure 6a1, the captured raw intensity image at z = 5 μm is coupled, that is, both the phase (such as Pharynx and Agar) and absorption (such as gonad) information can be seen simultaneously. While the focus plane is scanned quickly by the ETL, the phase information is cancelled, and the all-in-focus image is
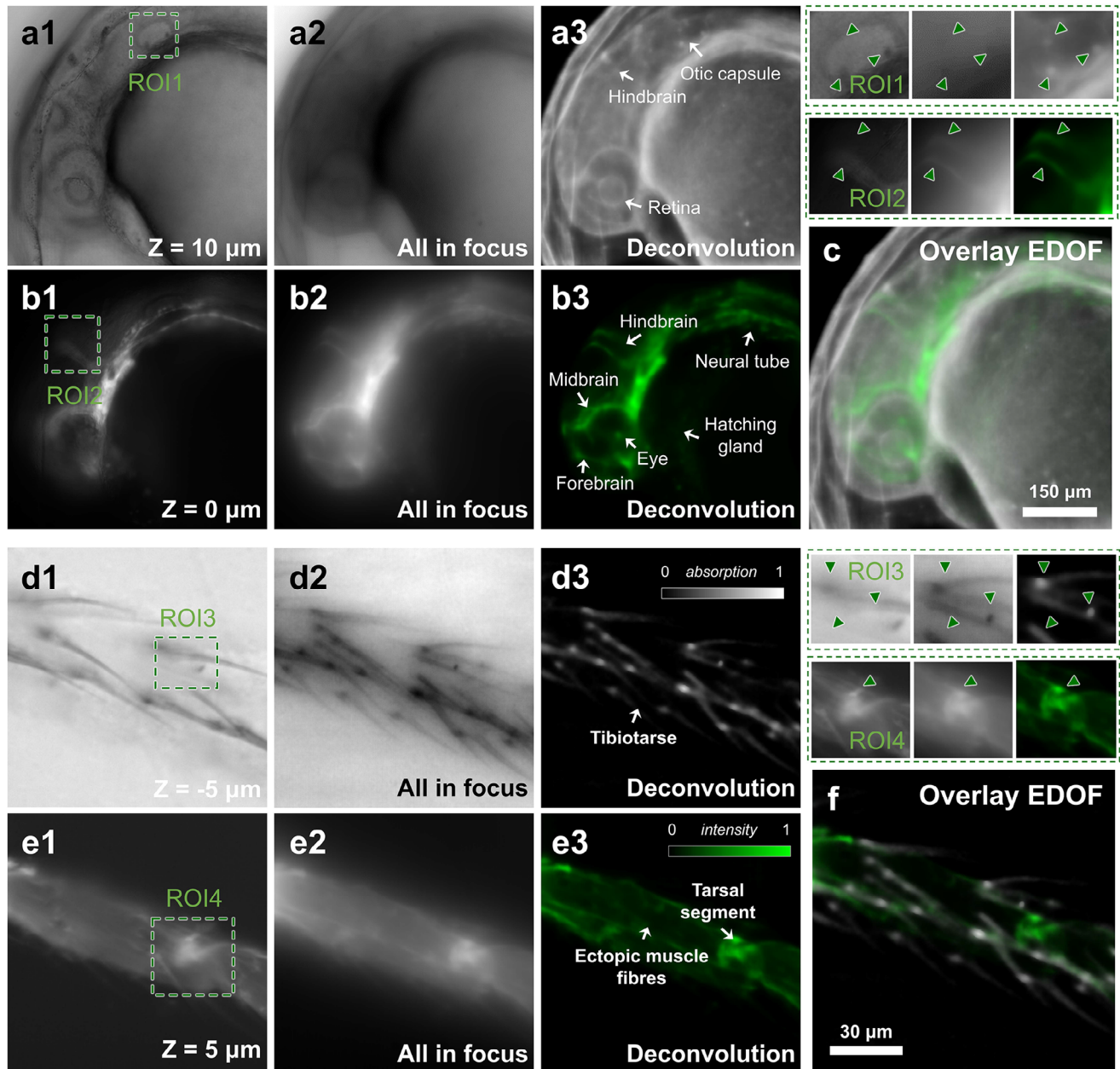
Figure 5. The dual-modalities EDOF experimental results of transgenic zebrafish *Tg(fli1:eGFP)* larvae and *Drosophila* larvae. a1) The raw image of zebrafish larvae under annular illumination modality at z = 10 μm. a2) The raw all-in-focus image. a3) The deconvolution result of a2. b1) The raw image of zebrafish larvae under wide-field fluorescent imaging modality at z = 0 μm. b2) The raw all-in-focus image. b3) The deconvolution result of b2. c, The dual-modalities overlay EDOF result of (a3) and (b3). Scalar bar 150 μm. d1) The raw image of the *Drosophila* larvae's leg under annular illumination modality at z = -5 μm. d2) The raw all-in-focus image. d3) The deconvolution result of (d2). e1) The raw image of *Drosophila* larvae's leg under wide-field fluorescent imaging modality at z = 5 μm. e2) The raw all-in-focus image. e3) The deconvolution result of (e2). f) The dual-modalities overlay EDOF result of (d3) and (e3). Scalar bar 30 μm.

left with absorption information, as shown in Figure 6a2. After deconvolution, the head and tail, which are mainly composed of phase information, are almost invisible, and the gonad becomes clear, as shown in Figure 6a3. With AI-EDOF's high-speed acquisition (~30 fps), we can monitor these all-in-focus absorption features in real-time (Figures 6b1–b3, Video S1, Supporting Information). On the other hand, our method also performs well un-

der the fluorescent imaging modality. We performed a heat shock (35°C for 20 min) on the *C. elegans*. As shown in Figure 6c1, the DOF of the raw image is limited at z = 2 μm, that is, the in-focus information is sharp, and the out-of-focus information is blurred. The all-in-focus image is captured by a quickly scanned ETL, as shown in Figure 6c2. After deconvolution, we can clearly see that the heat shock induces a clear translocation of the DAF-16
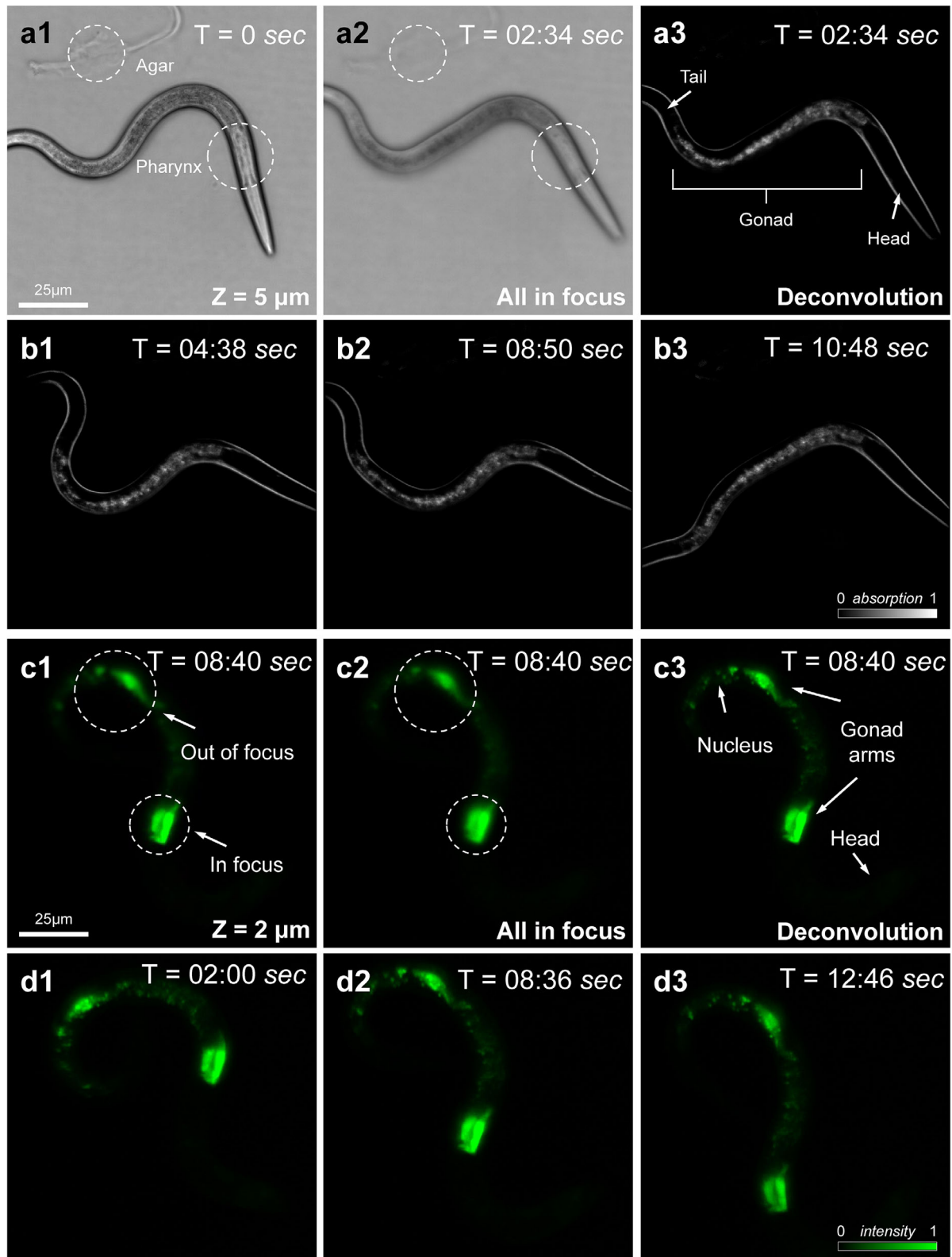
Figure 6. Dynamic multi-modalities EDOF experimental results of *C. elegans* (TJ356). a1) Raw image at z = 5 μm under annular illumination. a2) Raw all-in-focus image by focus scanning. a3) Deconvolution result of (a2). b1–b3) The absorption EDOF deconvolution results at different times (Video S1, Supporting Information). c1) Raw image at z = 2 μm under wide-field fluorescent imaging. c2) Raw all-in-focus image by focus scanning. c3) Deconvolution result of (c2). d1–d3) The fluorescent EDOF deconvolution results at different times (Video S2, Supporting Information). Scalar bar 25 μm.

transcription factor into the nucleus. Analogously, we performed a dynamic EDOF experiment on *C. elegans* under fluorescent imaging modality, as shown in Figures 6d1–d3 and Video S2, Supporting Information, and we can monitor the DAF-16 transcription over the whole volume. In the dynamic experiments, we first recorded raw images, and then post-processed the images frame by frame based on the RL deconvolution algorithm detailed in Section 2.3, and finally synthesized the results sequentially into a video file. These results highlight the potential utility of the AI-EDOF method for studying molecular biology and developmental biology.

4. Conclusion and Discussion

In this work, the effect of the source distribution of the formation of EDOF imaging in a partially coherent microscope has been explored. Compared with EDOF imaging using a conventional circular illumination aperture, it has shown that AI-EDOF, adopting the annular illumination matching the objective NA, allows for high contrast imaging with a lateral resolution close to the incoherent diffraction limit. Combined with a high-speed ETL located at the Fourier plane of the 4f telecentric module incorporated after the tube lens of the commercial inverted microscope, it is the first time that high spatial and temporal resolution motion-free all-in-focus imaging is demonstrated by our new approach. We quantitatively verified the resolution by a tilted USAF resolution target and demonstrated the capabilities of AI-EDOF by transgenic zebrafish larvae and *Drosophila* larvae. Moreover, we demonstrate the dynamic experimental results by *C. elegans* and showed that the absorption EDOF information can be decoupled. This technique is compatible with the conventional bright-field microscope (Köhler illumination), and can be easily combined with fluorescence techniques to gain labeled specificity, providing a wider window to investigate dynamic biological processes.[44–46]

However, some important issues still need to be clarified or require further investigation. First, the theoretical analysis and experimental results suggest that the coherence engineering of the illumination source provides new possibilities to extend the resolution limit and improve the low-frequency response of EDOF imaging. However, due to the complicated image formation of partially coherent imaging, solving for an optimum illumination source is quite challenging. Inspired by the benefits of annular illumination studied in various fields of microscopy[17,19,47–50] and microlithography,[51,52] we came up with the idea of improving the imaging contrast and resolution of EDOF through annular illumination. The current choice of annular aperture was empirically designed on the basis of intuitive criteria related to the shape of the 3D AOTF. Enabling the use of a more elaborate criterion (merit function) to evaluate the 'goodness' of an aperture and optimizing the aperture based on optimization algorithms are interesting directions for future work. Secondly, at present, the temporal resolution of our EDOF results is limited by the performance of sCMOS camera. The highest speed of ETL for focus scanning is up to ~1 kHz, while the frame rate of sCMOS camera is limited. On the other hand, the power of the LED light source and fluorescence excitation intensity restrict the exposure time. Although the noise can be suppressed to a certain extent by the RL-TV deconvolution method, a proper exposure time is still necessary. This problem may be further investigated by hardware upgrades (i.e., camera, light source). In addition to the acquisition speed, the acceleration of reconstruction algorithms is also a meaningful topic. Third, due to the possible aberrations of the imaging system, the practical PSF may differ from the simulated one. The algorithms for aberrations correction combined with RL deconvolution, such as blind deconvolution or adaptive optics,[53] will result in more accurate imaging reconstruction. Fourth, traditional CT techniques usually use coherent light sources (such as lasers) to illuminate the object to obtain a specific direction of projection under transmissive imaging, and the projection intensity is a slice of the Fourier spectrum. With the help of ETL, the intensity distribution of a 3D fluorescent sample can be integrated along the z-axis and 'projected' onto the 2D image plane. Consequently, the 'Fourier Slice Theorem', which only applies to coherent/partially coherent imaging before, can be extended to incoherent fluorescent imaging, as demonstrated in this paper and our previous work.[9] This is a promising direction for future work. Finally, our AI-EDOF method can only recover absorption EDOF information of the complex refractive index of the specimen, while EDOF for both phase and absorption information are important for diverse thick biological specimens in ODT. The phase information is eliminated because of the odd symmetry of POTF along the z axial, while this symmetry may be broken by asymmetric illumination, such as differential phase contrast imaging, which is also an interesting direction for future work.

Supporting Information

Supporting Information is available from the Wiley Online Library or from the author.

Conflict of Interest

The authors declare no conflict of interest.

Data Availability Statement

The data that support the findings of this study are available from the corresponding author upon reasonable request.

[1] E. R. Dowski, W. T. Cathey, *Appl. Opt.* **1995**, *34*, 1859.

[2] S. Bagheri, B. Javidi, *Opt. Lett.* **2008**, *33*, 757.

[3] J. Yang, L. Gong, Y. Shen, L. V. Wang, *Appl. Phys. Lett.* **2018**, *113*, 18.

[4] A. Levin, S. W. Hasinoff, P. Green, F. Durand, W. T. Freeman, *ACM Trans. Graph. (TOG)* **2009**, *28*, 97.

[5] M. Levoy, R. Ng, A. Adams, M. Footer, M. Horowitz, in *ACM Siggraph 2006 Papers*, ACM, New York **2006**, pp. 924–934.

[6] M. Broxton, L. Grosenick, S. Yang, N. Cohen, A. Andalman, K. Deisseroth, M. Levoy, *Opt. Express* **2013**, *21*, 25418.

[7] J. Wu, Z. Lu, D. Jiang, Y. Guo, H. Qiao, Y. Zhang, T. Zhu, Y. Cai, X. Zhang, K. Zhanghao, H. Xie, T. Yan, G. Zhang, X. Li, Z. Jiang, X. Lin, L. Fang, B. Zhou, P. Xi, J. Fan, L. Yu, Q. Da, *Cell* **2021**, *184*, 3318.

[8] Y. Zhang, Y. Wang, M. Wang, Y. Guo, X. Li, Y. Chen, Z. Lu, J. Wu, X. Ji, Q. Dai, *PhotoniX* **2022**, *3*, 1.

[9] Z. Cai, R. Zhang, N. Zhou, Q. Chen, C. Zuo, *Laser Photonics Rev.* **2023**, *17*, 2300217.

[10] S. Liu, H. Hua, *Opt. Express* **2011**, *19*, 353.

[11] E. J. Botcherby, R. Juskaitis, M. J. Booth, T. Wilson, *Opt. Lett.* **2007**, *32*, 14.

[12] H. Oku, K. Hashimoto, M. Ishikawa, *Opt. Express* **2004**, *12*, 2138.

[13] B. F. Grewe, F. F. Voigt, M. van't Hoff, F. Helmchen, *Biomed. Opt. Express* **2011**, *2*, 2035.

[14] W. J. Shain, N. A. Vickers, B. B. Goldberg, T. Bifano, J. Mertz, *Opt. Lett.* **2017**, *42*, 995.

[15] A. Mermillod-Blondin, E. McLeod, C. B. Arnold, *Opt. Lett.* **2008**, *33*, 2146.

[16] C. Liu, Z. Jiang, X. Wang, Y. Zheng, Y.-W. Zheng, Q.-H. Wang, *PhotoniX* **2022**, *3*, 20.

[17] C. Zuo, J. Sun, J. Li, J. Zhang, A. Asundi, Q. Chen, *Sci. Rep.* **2017**, *7*, 7654.

[18] C. Zuo, J. Li, J. Sun, Y. Fan, J. Zhang, L. Lu, R. Zhang, B. Wang, L. Huang, Q. Chen, *Opt. Lasers Eng.* **2020**, *135*, 106187.

[19] Y. Shu, J. Sun, J. Lyu, Y. Fan, N. Zhou, R. Ye, G. Zheng, Q. Chen, C. Zuo, *PhotoniX* **2022**, *3*, 24.

[20] L. Lu, J. Li, Y. Shu, J. Sun, J. Zhou, E. Y. Lam, Q. Chen, C. Zuo, *Adv. Photon.* **2022**, *4*, 056002.

[21] W. Choi, C. Fang-Yen, K. Badizadegan, S. Oh, N. Lue, R. R. Dasari, M. S. Feld, *Nat. Methods* **2007**, *4*, 717.

[22] Y. Sung, W. Choi, C. Fang-Yen, K. Badizadegan, R. R. Dasari, M. S. Feld, *Opt. Express* **2009**, *17*, 266.

[23] T. Kim, R. Zhou, M. Mir, S. D. Babacan, P. S. Carney, L. L. Goddard, G. Popescu, *Nat. Photonics* **2014**, *8*, 256.

[24] N. Zhou, J. Sun, R. Zhang, R. Ye, J. Li, Z. Bai, S. Zhou, Q. Chen, C. Zuo, *ACS Photonics* **2023**, *10*, 2461.

[25] J. Li, N. Zhou, J. Sun, S. Zhou, Z. Bai, L. Lu, Q. Chen, C. Zuo, *Light Sci. Appl.* **2022**, *11*, 154.

[26] S. Zhou, J. Li, J. Sun, N. Zhou, H. Ullah, Z. Bai, Q. Chen, C. Zuo, *Optica* **2022**, *9*, 1362.

[27] J. Park, D. J. Brady, G. Zheng, L. Tian, L. Gao, *Adv. Photonics* **2021**, *3*, 044001.

[28] X. Chang, L. Bian, J. Zhang, *eLight* **2021**, *1*, 1.

[29] N. Streibl, *J. Opt. Soc. Am. A* **1985**, *2*, 121.

[30] M. Chen, L. Tian, L. Waller, *Biomed. Opt. Express* **2016**, *7*, 3940.

[31] Z. Bai, Q. Chen, H. Ullah, L. Lu, N. Zhou, S. Zhou, J. Li, C. Zuo, *Opt. Lasers Eng.* **2022**, *156*, 107082.

[32] M. H. Jenkins, T. K. Gaylord, *Appl. Opt.* **2015**, *54*, 9213.

[33] J. M. Soto, J. A. Rodrigo, T. Alieva, *Opt. Express* **2017**, *25*, 15699.

[34] L. B. Lucy, *Astron. J.* **1974**, *79*, 745.

[35] W. H. Richardson, *J. Opt. Soc. Am.* **1972**, *62*, 55.

[36] J. W. Goodman, *Introduction to Fourier optics*, Roberts and Company publishers, Greenwood Village, CO, United States **2005**.

[37] C. Sheppard, A. Choudhury, *Int. J. Opt.* **1977**, *24*, 1051.

[38] H. H. Hopkins, *Proc. Math. Phys. Eng. Sci.* **1953**, *217*, 408.

[39] C. J. Sheppard, *J. Opt. Soc. Am. A* **2004**, *21*, 828.

[40] M. Born, E. Wolf, *Principles of Optics: Electromagnetic Theory of Propagation, Interference and Diffraction of Light*, Elsevier, Amsterdam **2013**.

[41] Y. Bao, T. K. Gaylord, *J. Opt. Soc. Am. A* **2016**, *33*, 2125.

[42] N. Dey, L. Blanc-Feraud, C. Zimmer, P. Roux, Z. Kam, J.-C. Olivo-Marin, J. Zerubia, *Microsc. Res. Tech.* **2006**, *69*, 260.

[43] C. Zuo, Q. Chen, W. Qu, A. Asundi, *Opt. Express* **2013**, *21*, 24060.

[44] Y. Park, G. Popescu, K. Badizadegan, R. R. Dasari, M. S. Feld, *Opt. Express* **2006**, *14*, 8263.

[45] D. Dong, X. Huang, L. Li, H. Mao, Y. Mo, G. Zhang, Z. Zhang, J. Shen, W. Liu, Z. Wu, G. Liu, Y. Liu, H. Yang, Q. Gong, K. Shi, L. Chen, *Light Sci. Appl.* **2020**, *9*, 11.

[46] J. Qian, Y. Cao, Y. Bi, H. Wu, Y. Liu, Q. Chen, C. Zuo, *ELight* **2023**, *3*, https://doi.org/10.1186/s43593-022-00035-x.

[47] F. Zernike, *Physica* **1942**, *9*, 974.

[48] T. Noda, S. Kawata, S. Minami, *Appl. Opt.* **1990**, *29*, 3810.

[49] B. Sick, B. Hecht, L. Novotny, *Phys. Rev. Lett.* **2000**, *85*, 4482.

[50] J. Sun, C. Zuo, J. Zhang, Y. Fan, Q. Chen, *Sci. Rep.* **2018**, *8*, 7669.

[51] K. Kamon, T. Miyamoto, Y. Myoi, H. Nagata, M. Tanaka, K. Horie, *Jpn. J. Appl. Phys.* **1991**, *30*, 3021.

[52] S. Heist, A. Mann, P. Kühmstedt, P. Schreiber, G. Notni, *Opt. Eng.* **2014**, *53*, 112208.

[53] C. He, J. Antonello, M. J. Booth, *ELight* **2023**, *3*, https://doi.org/10.1186/s43593-023-00056-0.